Broadband signal reconstruction for SHM

An experimental and numerical time reversal methodology

Falcetelli, Francesco; Venturini, Nicolas; Romero, Maria Barroso; Martinez, Marcias J.; Pant, Shashank; Troiani, Enrico

Important note
To cite this publication, please use the final published version (if applicable).
Please check the document version above.

Broadband signal reconstruction for SHM: An experimental and numerical time reversal methodology

Francesco Falcetelli[1,2] (iD)**, Nicolas Venturini[1,2], Maria Barroso Romero[3], Marcias J Martinez[2]** (iD) **, Shashank Pant[4] and Enrico Troiani[1]**

Abstract

Structural Health Monitoring (SHM) aims to shift aircraft maintenance from a time-based to a condition-based approach. Within all the SHM techniques, Acoustic Emission (AE) allows for the monitoring of large areas by analyzing Lamb waves propagating in plate like structures. In this study, the authors proposed a Time Reversal (TR) methodology with the aim of reconstructing an original and unaltered signal from an AE event. Although the TR method has been applied in Narrow-Band (NwB) signal reconstruction, it fails when a Broad-Band (BdB) signal, such as a real AE event, is present. Therefore, a novel methodology based on the use of a Frequencies Compensation Transfer Function (FCTF), which is capable of reconstructing both NwB and real BdB signals, is presented. The study was carried out experimentally using several sensor layouts and materials with two different AE sources: (i) a Numerically Built Broadband (NBB) signal, (ii) a Pencil Lead Break (PLB). The results were validated numerically using Abaqus/CAE^{TM} with the implementation of absorbing boundaries to minimize edge reflections.

1. Introduction

Structural Health Monitoring (SHM) research groups around the globe have developed several techniques for damage localization, quantification, and identification in critical assets (Farrar and Worden, 2007). In particular, Acoustic Emission (AE) has been identified as an effective method for detecting and localizing growing damages. AE events are commonly captured via Lead Zirconate Titanate (PZT) transducers, which can be surface-bonded or embedded in the structure (Moulin et al., 2000). The use of AE for damage detection is categorized as a passive method by the SHM community, since the sensors are only "listening" to the emitted signals along the structure (Balageas et al., 2006).

When elastic waves travel in a solid medium that is bounded on both sides, they are referred to as Lamb Waves (LW), in honor of Horace Lamb who studied them for the first time in 1917 (Lamb, 1917). LW can propagate for long distances with low attenuation and can be used to monitor wide areas in thin structures such as those typically found in aircraft structures (Cawley and Alleyne, 1996). These guided waves are described by the Rayleigh-Lamb Equations and propagate independently in two modes—the symmetric (S_n)

and the anti-symmetric (A_n) with different group velocities, where the subscript n represents the number of inflexion points found in the wave deformation field across the thickness (Pant et al., 2014).

In a traditional localization algorithm, the recorded Time of Arrivals (ToA) and the knowledge of the mode group velocities can be used to identify the origin of the AE source through triangulation algorithms. However, even if the localization scheme is relatively simple, determining and identifying the correct wave mode, hence the speed based on the ToA, can still be challenging when the wave packets contain multiple modes.

[1]Department of Industrial Engineering, University of Bologna, Forlì, FC, Italy
[2]Department of Mechanical and Aeronautical Engineering, Clarkson University, Potsdam, NY, USA
[3]Faculty of Aerospace Engineering, Delft University of Technology, Delft, Netherlands
[4]Aerospace Research Centre, National Research Council of Canada, Ottawa, ON, Canada

Corresponding author:
Francesco Falcetelli, Department of Industrial Engineering, University of Bologna, Via Fontanelle 40, Forlì, FC 47121, Italy.
Email: francesco.falcetelli@unibo.it

Recently, Barroso-Romero et al. (2019) published a paper discussing how the wave packets could be distinguished based on phase analysis. LW can be triggered by different types of damage in thin plate-like structures. For instance, in an isotropic material, a crack opening can be the source of an AE event (Roberts and Talebzadeh, 2003). On the other hand, in structures made out of composite material, delamination or fiber breakage generate AE signals, which are anisotropic in nature (Benmedakhene et al., 1999). In addition, other types of material degradation can also lead to AE events, such as: impacts (Diamanti et al., 2004), yielding (Dunegan et al., 1968), fretting (Wagle and Kato, 2009) and friction (Adler et al., 1990), etc. Hence, one of the primary challenges faced by the SHM community is attempting to numerically model these AE signals.

SHM researchers have developed several active techniques to excite LW in shell-like structures, to calibrate localization algorithms and to simulate AE events. The signals generated using such active methods can be categorized as Narrow-Band (NwB) and Broad-Band (BdB) signals. The Fast Fourier Transform (FFT) of a NwB signal is characterized by a single central frequency, whereas the FFT of a BdB signal contains a multitude of frequency peaks over a wide frequency range. The widely used NwB test signal is a Hanning Window (HW), introduced by Von Hann (1903). However, AE events generated by a damage in operational service environment are BdB in nature. Thus, several techniques were developed in order to mimic and reproduce the BdB AE signals, such as the use of the Pencil Lead Break (PLB) technique (ASTM International, 2010).

The PLB technique is of particular interest in this study since this technique has been chosen for the development of the numerical and experimental methodology developed herein. Hsu and Nielsen introduced the PLB technique in 1981 (Hsu and Breckenridge, 1981). Dunegan (2000) proved that the PLB technique was able to replicate the AE signals excited by noise sources (i.e. impact and friction) and by growing cracks in plate-like structures. Boczar and Lorenc (2006) showed that most of the energy of a PLB signal was concentrated below 350 kHz. In Sause (2011) it was demonstrated that different parameters can significantly change the characteristics of the emitted PLB signal such as the angle between the pencil lead and the test plate. As such, ASTM E-976 was written to document the implementation of the PLB technique (ASTM International, 2010).

Fink (1992) documented the first results on signal reconstruction through the use of ultrasonic waves, applying the Time Reversal (TR) concept to acoustic impulses in a pressure field. This technique was also known as the Time Reversal Mirror (TRM) since at the end of the process, the received signal is a time-reversed image of the input test signal. This methodology was implemented for the reconstruction of acoustic waves (Fink, 1997), and more specifically LW (Ing and Fink, 1998). Wang et al. (2003) tried to reconstruct a Gaussian pulse between two PZT transducers, making use of the frequency dependent time reversal operator introduced in the Mindlin Theory (Rose and Wang, 2004). This reconstruction was not completely successful since some discrepancies were noticed in the reconstructed signal with respect to the original Gaussian pulse signal. Then, Xu and Giurgiutiu (2007) reconstructed several HW signals exploiting the single mode and the two modes tuning effects of PZT transducers (Giurgiutiu, 2005). In that same year, Sohn et al. (2007b) utilized the wavelet transform in order to obtain an enhanced TR process for the signal reconstruction. Park et al. (2009) gave a theoretical interpretation to the presence of side bands observed during the reconstruction of HW signals in a two modes tuning modality. In Poddar et al. (2011) investigated the effect of different variables on the signal reconstruction through a TR process. The use of statistical damage classifier applied to the TR method has been evaluated in the delamination of composite plates (Sohn et al., 2007a). This technique was able to compensate the dispersive nature of LW and attracted the attention of many researchers thanks to its ability to reconstruct the emitted signal.

The idea of a Frequencies Compensation Transfer Function (FCTF) in combination with a virtual TR approach and absorbing boundaries for the signal reconstruction in plate-like structures was introduced in 2018 (Falcetelli et al., 2018). The absorbing boundaries were modeled in order to avoid edge reflections in numerical simulations and to reduce the model size which was fundamental to reduce the required computational cost. One of the most effective absorbing boundaries technique in Finite Element Model (FEM) is based on the Stiffness Reduction Method (SRM) (Pettit et al., 2014). Recently, Wang and Shen (2019) applied the FCTF technique with an experimental verification in order to reconstruct HW, thanks to a transducer transfer function through a virtual TR approach making use of absorbing boundaries.

The previously cited studies show that, so far, the TR approach for the signal reconstruction has been only successfully used with NwB waveforms. Indeed, Wang et al. identified discrepancies on the reconstructed Gaussian pulse signal because such signal is BdB in nature and thus covers a wide frequency range (Su and Ye, 2009). Moreover, it is important to note that during operational conditions it is impossible to generate a pure NwB signal due to the presence of background noise. Therefore, the primary focus of this study is to extend the TR technique to reconstruct a-priori known BdB signals and unknown BdB signals at their emanation site.

2. Methodology

This manuscript aims to perform BdB signal reconstruction as an extension of two recent studies (Falcetelli et al., 2018; Wang and Shen, 2019). The goal of this study is to demonstrate the experimental/numerical/hybrid method and validate the methodology on the reconstruction of two signals: the Numerically Built Broadband (NBB) and the PLB signals. The NBB signal reconstruction was used to prove the applicability of the FCTF TR method to BdB signals, which are known a-priori, while the PLB signal reconstruction extended the application to unknown BdB signal sources. In this study, Band Limited White Noises (BLWN) were used as a mean for building the FCTF. Another important aspect of this study is the variety of sensors types, configurations and materials used to assess and prove the proposed methodology for different configurations.

The methodology used in this study has been divided into three phases for clarity.

  I.   Analytical description of the TR method for BdB signals: The application of a FCTF to the TR method is described mathematically, thereby developing a strategy to reconstruct a generic BdB signal.
 II.   Experimental application: The FCTF TR process is applied experimentally to reconstruct NBB and PLB signals on a thin aluminum plate (1.6 mm thick), followed by the reconstruction of NBB signals on a thick steel plate (13 mm thick).
III.   Computational verification: Validation of the technique presented in this work was performed through the development of a numerical model using Abaqus/CAE$^{\text{TM}}$. The TR process was applied to NBB and PLB signals.

2.1. Analytical description of the TR method for BdB signals

Figure 1 shows the TR process applied to a generic signal propagating in a plate-like structure.

Referring to Figure 1, the input signal (a), the recorded signal (b), the new input signal (c), and the output signal (d) are denoted by $V_i(t)$, $V_R(t)$, $V_R(-t)$, and $V_A(t)$ in the time domain respectively. Applying the Fourier Transform operation, $\mathcal{F}$, one obtains the signals spectra $\widehat{V}_i(\omega)$, $\widehat{V}_R(\omega)$, $\widehat{V}_R(\omega)^*$, and $\widehat{V}_A(\omega)$, respectively, where ω indicates their frequency dependency and the superscript (*) represents a complex conjugate. The bijective property of the Fourier Transform allows

to retrieve the signals time-dependent form, through an inverse operation ($\mathcal{F}^{-1}$). The forward signal propagation between PZT A (Actuator) and PZT R (Receiver) is affected by the frequency dependent function $G(\omega)$, whereas the backward signal propagation between PZT R and PZT A depends on its complex-conjugate form $G(\omega)^*$. Recent studies (Falcetelli et al., 2018) and (Wang and Shen, 2019), provided the analytical expression of the time-reversed version of the output signal $V_A(t)$ as expressed in equation (1).

$$V_A(-t) = \mathcal{F}^{-1}\left[\widehat{V}_i(\omega) \cdot |G(\omega)|^2\right] \qquad (1)$$

In this study, the quantity $|G(\omega)|^2$ will be called Frequency Compensation Transfer Function (FCTF). The FCTF depends on the system and distorts the original signal and acts as a filter whose gain is frequency dependent. Equation (1) illustrates the mathematical relation between the time reversed signal received at PZT A, $V_A(t)$, and the original signal in the frequency domain, $\widehat{V}_i(\omega)$. The novel aspect of this study is the development of a methodology to derive the FCTF and then applying it within the TR method for the reconstruction of BdB signals.

2.1.1. FCTF derivation and BdB signal reconstruction.
The TR method exploits the spatial reciprocity and the time reversal invariance of the propagating waves (Fink, 1992, 1997). Nevertheless, when these concepts are applied to LW, the result is affected by their dispersive nature (Ing and Fink, 1998). Their interaction with the system is frequency dependent and is described by the FCTF. The FCTF determines how each frequency component of the input signal is scaled during the TR process (Wang et al., 2003). The novel strategy applied in this study is to use the TR process itself, by injecting a test function into the system and observing the changes in its spectrum. The test function should stimulate every frequency component. A pure white noise signal represents the perfect test signal since it has a wide and constant power density spectrum. However, a pure white noise signal is unrealistic from an experimental, as well as, a computational point of view as an infinite bandwidth is not necessary for SHM applications. Therefore, it was decided to use a Band Limited White Noise (BLWN) signal, $V_{BLWN}(t)$ as a test function. Hence, according to equation (1) the received time reversed signal at PZT A becomes:

$$V_A|_{BLWN}(-t) = \mathcal{F}^{-1}\left[\widehat{V}_{BLWN}(\omega) \cdot |G|_{BLWN}(\omega)|^2\right] \qquad (2)$$

Where $\widehat{V}_{BLWN}(\omega)$ represents the spectrum of the input signal $V_{BLWN}(t)$. Then, applying the Fourier Transform,
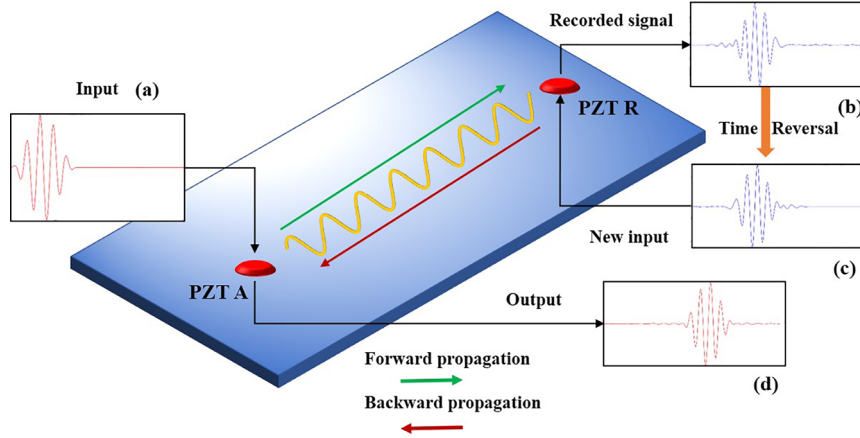
Figure 1. TR process applied to a generic signal in a plate-like structure.

and dividing by the spectrum of the BLWN signal $\hat{V}_{BLWN}(\omega)$, it is possible to derive the FCTF as follows:

$$\left|G|_{BLWN}(\omega)\right|^2 = \frac{\hat{V}_A^*|_{BLWN}(\omega)}{\hat{V}_{BLWN}(\omega)} \qquad (3)$$

Considering the FCTF as the known function given by $\left|G|_{BLWN}(\omega)\right|^2$, it is possible to reconstruct the original input signal, for the BdB signal. Starting from equation (3), substituting $\hat{V}_{BLWN}(\omega)$ with the spectrum of a generic BdB input signal $\hat{V}_i|_{BdB}(\omega)$ and multiplying both sides by $\hat{V}_i|_{BdB}(\omega)$ one obtains:

$$\hat{V}_A^*|_{BdB}(\omega) = \hat{V}_i|_{BdB}(\omega) \cdot \left|G|_{BLWN}(\omega)\right|^2 \qquad (4)$$

The original input signal can be derived dividing both sides of equation (4) by the FCTF (equation 3) and taking the Inverse Fourier Transform as outlined in equation (5):

$$V_i|_{BdB}(t) = \mathcal{F}^{-1}\left[\frac{\hat{V}_A^*|_{BdB}(\omega)}{\left|G|_{BLWN}(\omega)\right|^2}\right] \qquad (5)$$

As such, the original signal is equal to the Inverse Fourier Transform of the ratio between the spectrum of the time reversed signal received at PZT A and the FCTF.

The theoretical expressions derived above describe a generic BdB signal and involves two PZT transducers. Lamb waves propagate with a circular front in isotropic materials. In practical applications a minimum of three to four PZT transducers around the emitting signal are used for capturing the signal and for localization. However, a higher than the minimum number of PZT transducers translates into a higher number of collected signals. Sending back those signals at the emanation site will result in a better energy re-focusing (Anderson et al., 2008). Indeed, the Lamb Waves emitted by each transducer will intersect at the emanation site leading

to LW amplification and thus to higher energy at the end of a TR process. Theoretically, an infinite number of receivers leads to a perfect reconstruction (Anderson et al., 2008; Cassereau and Fink, 1992). Several studies have used large number of transducers for TR process such as the one by Ing and Fink (1998), which employed more than 30 transducers. This is because energy-based localization algorithms require a high number of PZT transducers for a better precision (Su and Ye, 2009). However, high number of PZT transducers are unpractical for real SHM applications and optimizing the sensor networks for a given system is an active area of research (Su and Ye, 2009). For this reason, no more than five transducers were used in this study. The process would be identical to the two PZT sensors case with the only difference being, once the signal is recorded by the n receivers, it is sent back simultaneously to the central actuator capturing the superposition of all the retransmitted signals. In regards to the $V_i(t)$ signal length, there is no specific requirement. The selection of the length of these signals depends on several factors, such as: targeted wave modes and their TOA, computational cost for numerical simulation, required accuracy, and geometric limitations to minimize errors due to wave reflections. Therefore, in this study the authors used signal up to 120 μs for reconstruction, which is in line with what is found in the current literature (Park et al., 2009; Wang and Shen, 2019).

2.2. Experimental application

2.2.1. Plates and sensor networks. The experimental setup consisted of a 7075-T6 aluminum plate measuring 304.8 mm $\times$ 609.6 mm $\times$ 1.6 mm with a Young's modulus of 71.7 GPa, a Poisson's ratio of 0.33 and the density equal to 2810 kg/m^3. For this configuration, the fundamental S_0 and A_0 modes were present below 1 MHz. The plate was surrounded with a vacuum bag sealing
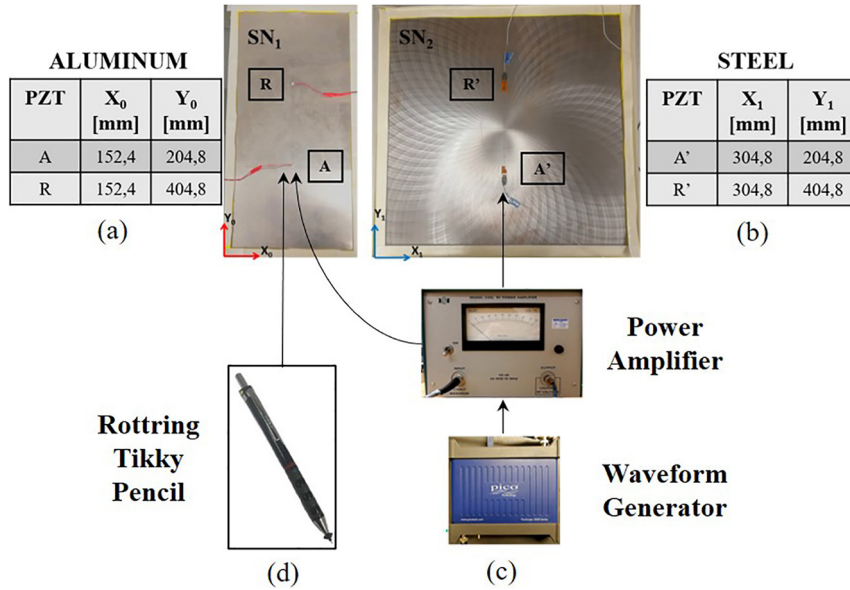
Figure 2. Experimental sensor networks SN_1 (Al) and SN_2 (Steel).

tape to dampen the wave in order to reduce / eliminate any reflections from the plate boundaries. A network of two Piezokinetic Sensors labeled as PZT A and PZT R were used on the aluminum plate similar to what was introduced in the analytical section. The sensors had a diameter of 0.253 inches, thickness of 0.032 inches, a mechanical quality factor of 500, a loss factor $\tan\delta$ equal to 1.5% and the dielectric constant K^T was 1744 (Piezo-Kinetics, 2016). The positions of these transducers are shown in Figure 2(a), where SN_1 denotes the experimental sensor network setup for the aluminum plate. The experimental methodology for the BdB signal reconstruction, was also applied to an A572 low carbon steel plate measuring 609.6 mm x 609.6 with a thickness of 13 mm with two PZT sensors from *Acellent* Inc. The sensors had a dielectric constant K^T equal to 1275, a loss factor $\tan\delta$ equal to 0.60%, and a mechanical quality factor of 500 (APC International, 2019). The measured resonance and anti-resonance peaks were around 300 kHz and 350 kHz, respectively. This second configuration, denoted SN_2, is shown in Figure 2(b). The two setups allowed the authors to validate the developed methodology on different type of materials and sensors. For both configurations, the PZTs were bonded to the plates with the Momentive Silicone Rubber, which was cured for 24 h prior to testing. Silicon is often used in SHM applications in order to fix PZT transducers as in (Martin and Blackshire, 2007) and (Mulligan et al., 2011) for example.

The signal captured by the PZT transducer working as a sensor was first amplified by 36 dB using an AEPH5 Pre-Amplifier and then saved onto AMSY-6 AE-measurement system from Vallen AE-Measurement Système. The raw signal without any application of analog filter was captured at a sampling frequency of 5 MHz.

2.2.2. Experimental FCTF derivation. The FCTF methodology was applied to the S_0 wave packet (fastest mode for the used frequency range). The FCTF creation procedure is explained in the following steps for the SN_1 configuration:

(a) A Band Limited White Noise (BLWN) bounded between $[-1,1]$ with zero mean value and a standard deviation of 0.1 was generated in Matlab^{TM}. The signal was filtered using a sixth-order Butterworth low-pass filter up to 1 MHz. Such BLWN signal is represented in Figure 3 with its amplitude spectrum.

(b) Then, an amplified version of the BLWN signal up to 40 V was used as input signal $V_{BLWN}(t)$ to the system as shown in Figure 1(a) through PZT A. The experimental setup, shown in Figure 2(c), was composed of a waveform generator Picoscope 3204-DMSO, the Broadband Power Amplifier ENI 240L and a PZT actuator fixed onto the plate, allowing for the amplification and emission of the signals.

(c) PZT R receives a distorted version of the input signal, $V_R(t)$ as shown in Figure 1(b). The S_0 wave packet of the received signal was isolated, re-sampled, normalized and time-reversed in Matlab^{TM}. The time reversed signal is represented by $V_R(-t)$.

(d) The time-reversed signal was then amplified up to 40 V and sent back. In this step, the roles of the PZT transducers were switched, PZT R

became the actuator while PZT A became the sensor as shown in Figure 1(c).

(e) PZT A received an output signal $V_A(t)$ which was a distorted version of the time-reversed signal as shown in Figure 1(d). The S_0 wave packet of the output signal was isolated, normalized, and time-reversed. The time-reversed output was then $V_A(-t)$.

A cross-correlation was performed between the input signal $V_{BLWN}(t)$ and the time-reversed output signal $V_A(-t)$ in order to align these two signals. Furthermore, the ratio between the FFT of these two signals was calculated. The FFT ratio of the cross-correlated signals of the previous step allowed to obtain a set of data points representative of the FCTF as stated in equation (3). The procedure was repeated ten times in order to obtain a cloud of data to interpolate with a smoothing spline, and thus a reliable trend of the FCTF could be obtained.

2.2.3. Signal sources on the aluminum plate. Two BdB signals have been chosen to act as a source at the same location of PZT A. These signals are denoted by $V_i(t)$ in the analytical description of the TR method for BdB signals.

The first BdB signal consisted of a NBB signal of $30 \mu s$ in a frequency range below 1 MHz. This signal was produced in Matlab^{TM}, with an amplitude normalized between $[-1, 1]$ using the random signal generator command. The setup, which is shown in Figure 2(c), allows for the emission of an amplified version of the NBB signal up to 40 V. The second BdB signal was the PLB signal. The PLB signal was generated by breaking the graphite lead of the Rottring Tikky Pencil at the same location of PZT A following the modalities specified in the ASTM E-976 (ASTM International, 2010) and is shown in Figure 2(d).

2.2.4. Signal reconstruction and verification on the aluminum plate. The signal reconstruction process represents the last section of the experimental methodology. First, the four sub-steps (b through e) of section 2.2.2. are repeated with each of the two signal sources $V_i(t)$ introduced in section 2.2.3. If the signal source is a NBB signal, the input signal is amplified up to 40 V, to be consistent with the FCTF creation process.

Applying the FCTF obtained in Section 2.2.2 from the BLWN signal, to the time-reversed output signal $\hat{V}_A^*(\omega)$ and performing an inverse Fourier transform, as shown in equation (5), allows to obtain the original input signal $V_i(t)$. Nevertheless, the original input signal obtained from equation (5) as described, will be denoted with $V_{REC}(t)$ in order to distinguish between the theoretical $V_i(t)$ and the experimentally reconstructed signal.

For the case of a known input source signal, such as the NBB signal, it is possible to make a comparison between $V_i(t)$ and $V_{REC}(t)$ to verify the effectiveness of the proposed method. On the other hand, for the case of an unknown input source, such as the PLB signal emitted on the SN_1 configuration, it is impossible to apply the same procedure since the input signal $V_i(t)$ is unknown. Therefore, to verify if the hypothetical reconstructed signal $V_{REC}(t)$ matches with the unknown input signal $V_i(t)$, $V_{REC}(t)$ was sent as input signal from a PZT A (amplifying the signal up to 40 V). A distorted version of the reconstructed signal $V_{R-REC}(t)$ is received at PZT R. Finally, to verify the effectiveness of the method, $V_{R-REC}(t)$ was compared with $V_R(t)$, distorted version of the actual PLB.

2.2.5. Signal reconstruction and verification on the steel plate. The same experimental methodologies described in Sections 2.2.2 to 2.2.4 were applied to the configuration SN_2, with the exception that only the NBB signal was used as input signal $V_i(t)$ and reconstructed for this case. Some differences have to be highlighted with respect to the case of the aluminum plate:

- The dispersion curves of this steel plate were such that the fundamental S_0 and A_0 modes propagated below 150 kHz whereas the high order modes propagated at frequencies higher than 150 kHz. In particular, the S_1 mode is the fastest mode at 350 kHz.
- As a consequence of the previous point, the experimental FCTF derivation and the experimental reconstruction process do not rely only on the S_0 mode, but on the first arriving wave packet which can be interpreted as a wave packet composed by multiple modes propagating at similar speeds as for example S_0, S_1 and S_2 propagating in between 4700 and 4800 km/s at approximately 100, 300, and 550 kHz, respectively.
- The sensor configuration SN_2, related to the steel plate, is introduced in Figure 2(b). The location of the Acellent Sensors on the steel plate is different with respect to the SN_1 configuration in Figure 2(a) because the two plates have different dimensions.

The reconstructed signals duration was 30 μs for both aluminum and steel cases. This duration was principally set by the Picoscope Waveform Generator sample limitation which depends on the arbitrary waveform generator buffer size (PicoTechnology, 2016). As previously explained, the signal must be re-sampled before its amplification. That is why a trade-off was necessary between the signal length and the signal sampling.

2.3. Computational verification

The numerical simulations were performed in a Windows 10 workstation with 2 Intel® Xeon® CPU E5-2620 v3 (12 cores and 24 logical) running at 2.40 GHz. Wave damping was modeled in order to consider attenuation. Moreover, the implementation of absorbing boundaries using the SRM was studied to avoid edge reflections and to obtain a clean undisturbed signal. The numerical model was developed using ABAQUS CAE^{TM}, where the modeling of piezoelectric elements requires the use of an implicit software, which can be extremely time consuming for high frequencies signals.

2.3.1. Modeling of the plate, piezoelectric transducers and sensor network.

The 7075-T6 aluminum plate dimensions and mechanical properties already introduced in section 2.2.1 were modeled in ABAQUS CAE^{TM}. The wave damping model, the absorbing boundaries, and the mesh considerations are discussed in the next sections. The selected sensor VS900-M Vallen Système is a passive piezoelectric AE sensor with broad frequency response (Vallen Systeme, 2019), as shown in Figure 4. The PZT actuator and sensors used in this study were single sensors simulated as cylindrical disks of 6.5 mm in diameter with a thickness of 0.25 mm. The piezoelectric actuator/sensors were assigned orthotropic Piezoelectric Navy I material with the following properties: $E_{11} = E_{22} = 80$ GPa; $E_{33} = 68$ GPa; $G_{13} = G_{23} = 30.5$ GPa; $G_{12} = 29.0$ GPa; and Poisson's Ratio $v_{12} = v_{31} = v_{32} = 0.31$. The piezoelectric charge constants were set to: $d_{31} = -125 \times 10\text{-}12$ C/N; $d_{33} = 290 \times 10\text{-}12$ C/N; and $d_{15} = 480 \times 10\text{-}12$ C/N. Finally, the relative dielectric constants were assigned values of $k_{11} = k_{22} = 1275$, and $k_{33} = 1320$ ($\varepsilon_o = 8.85410\text{-}12$ F/m), while the density was set to 7600 kg/m^3 (Martinez et al., 2017). Five PZT sensors composed the sensor network chosen for this verification. The center of the plate represents the location of the actuation and reconstruction of the different signals, PZT A. Figure 4(a) shows the new experimental layout, (b) the sensor coordinates, and (c) the corresponding numerical model. In the experimental setup of Figure 4(a) the sensors were fixed with the Momentive Silicone Rubber. This coupling was modeled imposing a tie constraint in the numerical model.

Absorbing boundaries were implemented to avoid edge reflections using the stiffness reduction method introduced by Pettit et al. (2014). Moreover, wave damping was modeled according to the methodology proposed by Gresil and Giurgiutiu (2015) in their study.

2.3.2. Mesh and time steps considerations.

The element size and time step set in this model followed those proposed by Bhuiyan et al. (2018) and Moser et al. (1999), which guarantees sufficient mesh refinement ($l_e = 0.25$ to 0.4 mm) and time step resolution ($\Delta t = 12.5$ nano-seconds) to avoid aliasing of the acoustic signals. The number of elements associated to the model mesh were between 1,909,908 and 3,573,738 elements. The elements types used in this study consisted of C3D8R for the plate structure and C3D8E for modeling the piezoelectric elements.

2.3.3 Numerical FCTF derivation.

Similarly, to the experimental FCTF derivation, the numerical FCTFs are derived using a BLWN signal $V_{BLWN}(t)$ as input signal in the ABAQUS CAE^{TM} model. This BLWN was generated using a MATLAB^{TM} code with a zero mean value and a standard deviation of 0.1. The signal length was set to 50 μs and mapped within the interval $[-1,1]$. In the experimental setup, the PLB spectrum was found to have most of its energy in the range from 50 kHz to 400 kHz. Therefore, a sixth order Butterworth low-pass filter of 400 kHz was applied to the previously generated white noise in order to obtain a BLWN. However, the upper limit of the cut-off frequency depends also on the available computational power as higher frequencies translates into smaller time steps and consequently increase in computational time. The BLWN signal is similar to the one represented in Figure 3 with one difference being that the cut-off frequency was set at 400 kHz.

The BLWN signal $V_{BLWN}(t)$ was then imposed as an electric potential at the top surface of the central PZT (actuator Sensor 5) of the FE model, with a maximum positive value of 10 V. Following steps (b) to (e) in section 2.2.2 within the FE model, equation (5) finally provides the sought FCTF.

2.3.4. Implementation of the test signals in the FEM model.

Two BdB signals, the NBB signal and the PLB signal already introduced in Section 2.2.3 have been chosen to act as a source or input signal $V_i(t)$, at the location of the central PZT.

Since the NBB input signal is known a-priori, the $V_i(t)$ was directly injected in PZT A or the central PZT actuator of the FEM model. As a consequence, four NBB signals $V_R(t)$ were captured by the four non-central PZT of the FEM model and these signals were time-reversed to obtain $V_R(-t)$.

On the other hand, the PLB source signal was unknown and a direct implementation through the central PZT of the FEM models was impossible. The solution was to perform experimentally the PLB test on the center of the plate. Then, four PLB signals $V_R(t)$ were captured experimentally by the four non-central sensors. Finally, the experimentally captured signals were time-reversed, obtaining four $V_R(-t)$ signals that were injected in the four non-central PZT of the FEM model.

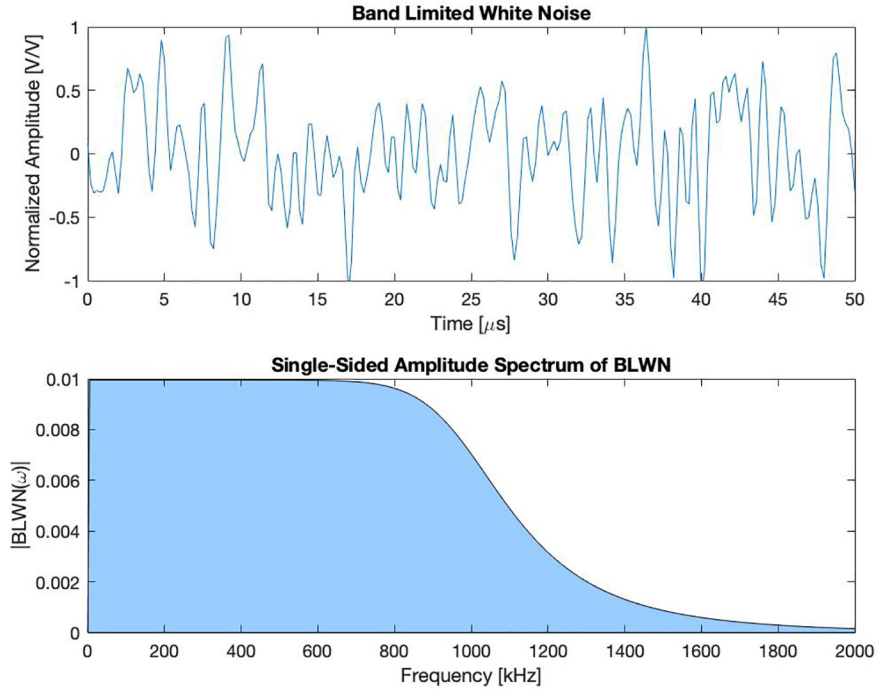At this point, the reconstruction and verification process were similar to the experimental process. For

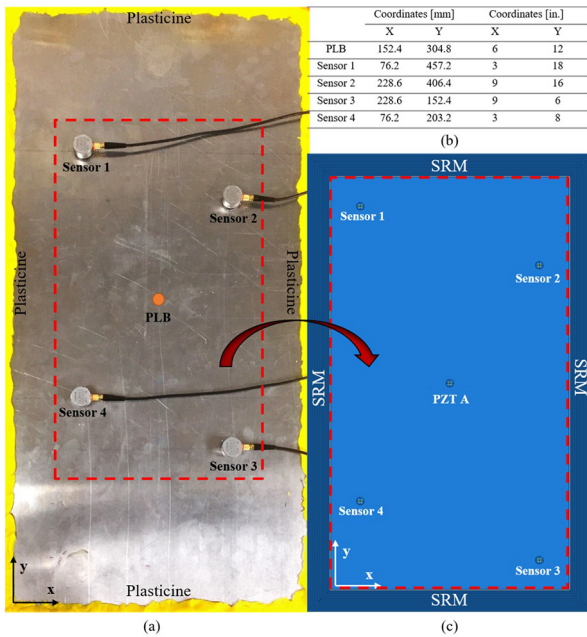**Figure 3.** Experimental BLWN signal and its single-sided amplitude spectrum.

**Figure 4.** Numerical approach configuration.

both NBB and PLB cases, the four time-reversed signals $V_R(-t)$ were injected in the plate of the FEM model through the four non-central PZT. Successively, the central PZT received the $V_A(t)$ signal in both NBB and PLB cases. Applying the FCTFs to the time-reversed FFT of $V_A(t)$ allows to obtain the reconstructed signal $V_{REC}(t)$ in the FEM models.

It is worth noting that in both cases, the signals have been reconstructed for both S_0 and A_0 modes and not only with the S_0 mode as in the experimental case. Indeed, the efficient wave absorption action introduced by the SRM boundaries allows obtaining S_0 and A_0 modes in the FEM model, and both modes can be used for the BdB signal reconstruction. Moreover, the reconstructed signals are no longer than 100 and 120 µs for the NBB and PLB cases respectively. This limitation allowed to restrict the computational cost by limiting the signal samples while considering more than a single wave packet differently from the experimental part.

As in the experimental verification for the NBB case, the effectiveness of the numerical reconstruction can be demonstrated by comparing $V_i(t)$ with $V_{REC}(t)$, since $V_i(t)$ is known a-priori in the NBB case. Nevertheless, $V_i(t)$ is not known a-priori for the PLB case. Therefore, the verification is performed by injecting $V_{REC}(t)$ through the central PZT of the FEM model. Then, four signals $V_{R-REC}(t)$ are captured at the four non-central PZT of the FEM model. These four signals can be compared with the four signals $V_R(t)$ obtained experimentally in section 2.2.4 to assess the effectiveness of the reconstruction. Figure 5 introduces a flow-chart summarizing the different steps applied for the experimental and numerical/hybrid BdB signal reconstruction.

3. Results and discussion

The objective of this study was to apply the same methodology in different scenarios and verify its
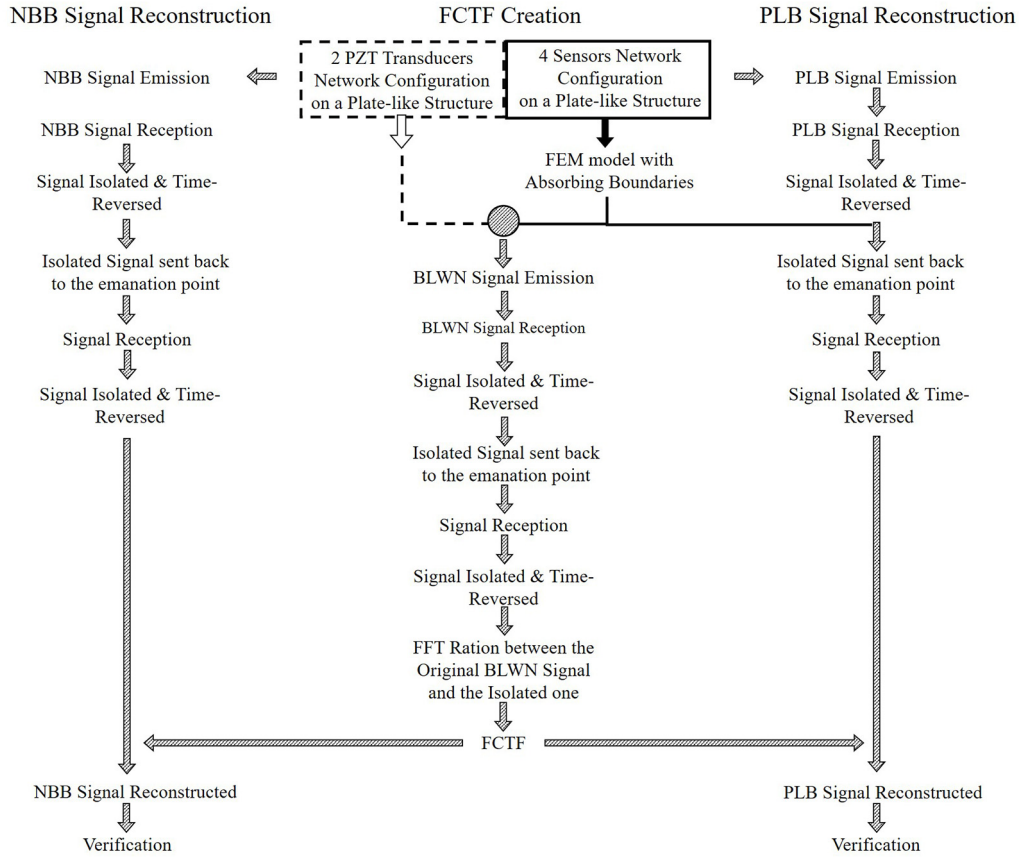
Figure 5. Experimental (dashed line) and Numerical/Hybrid (solid line) methodology flow-chart for BdB Signal Reconstruction.

effectiveness and generality. The independence of the methodology from the specific material used, sensors and geometry are of crucial importance to extend this approach to real SHM applications. It is worth noting that the length of the reconstructed signals in this study ranges between 25 and 120 μs. This interval was set in order to answer primarily to the technical issues of the waveform generator as explained in the methodology, compensating with sampling for sufficient level of accuracy. Nevertheless, such time interval is in line with other well-known studies making use of the TR approach such as (Park et al., 2009) and (Wang and Shen, 2019). The primary step was to demonstrate the methodology effectiveness regardless of the signal length. The application of the FCTF methodology to longer signals could represent an interesting issue to solve in the future. This could extend the generality of the FCTF methodology and represent a step further for real SHM application.

3.1. Aluminum and steel frequencies compensation transfer functions

Applying the experimental methodology of Section 2.2.2, two sets of data for the aluminum and steel plates were obtained. The aluminum and steel FCTFs were

derived using a smoothing spline interpolation on Matlab^{TM}. The aluminum FCTF is represented in Figure 6(a); whereas Figure 6(b) introduces the steel FCTF. The red dotted line separates the region of attenuation and amplification of the frequencies in both figures.

In the aluminum plate, the experimental FCTFs were developed based on the TR process of the first arriving wave packet at the PZT sensors using as input signal a BLWN having the maximum frequencies below 1 MHz. According to this, the aluminum FCTF of Figure 6(a) is built based on the TR process of the S_0 wave packet because the S_0 mode is the fastest mode below 1 MHz. However, for the steel plate the development of the FCTF is more complicated due to the presence of multiple Lamb wave modes. In this frequency range, several high order modes propagate at similar speeds in the steel plate such as S_0, S_1, and S_2 propagating in between 4700 and 4800 km/s at approximately 100, 300, and 550 kHz, respectively. As a consequence, it can be implied that the experimental steel FCTF of Figure 6(b) is based on the TR process of a wave packet composed by multiple modes propagating at similar speeds.

In comparing the experimental FCTFs obtained for aluminum and steel plates, these FCTFs show a similar
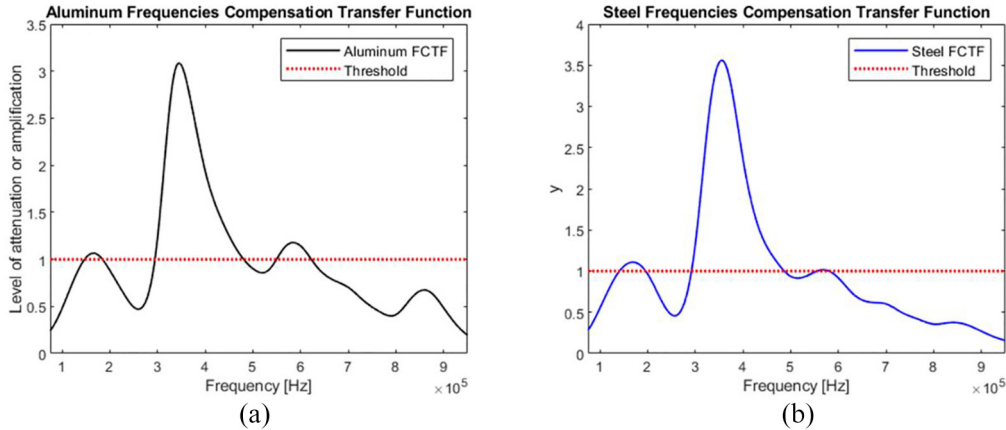
Figure 6. (a) Aluminum FCTF and (b) Steel FCTF.
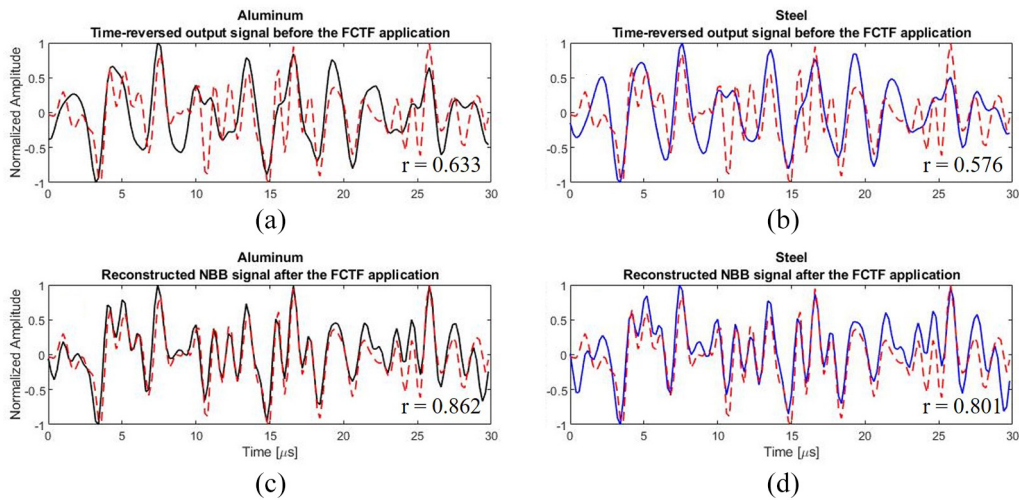
Figure 7. Comparisons between: (a) the original and the reconstructed NBB signals before the FCTF application in the aluminum plate, (b) application in the steel plate, (c) the original and reconstructed NBB signals after the FCTF application in the aluminum plate, and (d) in the steel plate.

trend with a main amplification peak localized between 300 kHz and 400 kHz as shown in Figure 6(a) and (b) respectively. These similar trends seem to indicate that the FCTF is material independent. In addition, it is important to note that the dimensions of the plate and the sensor type used in both experimental setups were different. The authors believe that variables such as the impedance could potentially play an important role in the FCTF derivation and explain the experimental FCTF similarities. Indeed, taking as an example the Acellent sensors, their impedance valley and peak, corresponding to their resonance and anti-resonance frequencies respectively, are within the frequency range between 300 and 400 kHz. The same frequency range contains the FCTF peak. If such hypothesis turns out to be true, then this conclusion could underline the importance of the PZT Transducer in the system and strengthen the study of Wang and Shen (2019) which

made use of a Transducer Transfer Function in order to compensate the frequencies. Moreover, the importance of the silicone adhesive must not be underestimated. Qing et al. (2006) demonstrated the adhesive effect on the PZT transducers performances, in particular on the impedance.

3.2. Numerical broadband signals reconstruction

The first experimental reconstruction was performed for a NBB signal. Figure 7 introduces the steps of the NBB signal reconstruction process. The red-dotted line represents the original input NBB signal, $V_i(t)$. In particular, Figure 7(a) and (b) show the $V_A(-t)$ reconstructed NBB signals before the FCTFs application in black and blue for the aluminum and steel cases respectively. Figure 7(c) and (d) represent the reconstructed NBB signals after the application of FCTF according

to equation (5) in black and blue for the aluminum and steel cases respectively. Finally, the correlation coefficient "r" is introduced in each case.

In the experimental NBB signal reconstruction for the aluminum plate, the NBB signal contains frequency peaks until 1 MHz which means that both the S_0 wave packet and the A_0 wave packet propagated on the aluminum plate. However, the reconstruction of the NBB signal in the aluminum plate is based only on the S_0 wave packet which is the fastest mode. Moreover, the application of the aluminum FCTF allowed for an improvement of the NBB signal reconstruction in terms of correlation coefficient passing from the time-reversed output signal $V_A(-t)$ in Figure 7(a) to the reconstructed signal $V_{REC}(t)$ in Figure 7(c), with a correlation coefficient improvement of 36%. Thus, this result confirms that the reconstruction of a NBB signal through the FCTF method can be performed based on the TR process of a single wave packet.

However, for the experimental NBB signal reconstruction on the steel plate, other considerations were made. As the NBB signal contains frequency peaks up to 1 MHz, the propagation of different wave packets with similar speeds occurs in the steel plate, such as for example the S_0, S_1, and S_2 propagating in between 4700 and 4800 km/s at approximatively 100, 300 and 550 kHz, respectively. This indicates that the first arriving wave packet at the PZT transducer is of difficult interpretation and could be a combination of several high order modes traveling at a similar speed. Nevertheless, the reconstruction is still viable in this case. This could be observed as the trend of the original signal is kept after the application of the FCTF with an improvement of approximately 39% on the correlation coefficient as shown in Figure 7(b) and (d). It is possible to associate this reconstruction improvement in the steel plate with the creation process of the steel FCTF due to TR process of a multi-mode wave packet signal.
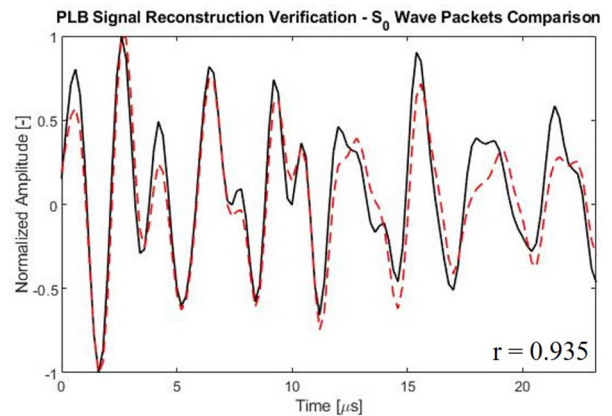
3.3. PLB signal reconstruction

The S_0 wave packet of the time-reversed output signal $V_A(-t)$ at the end of the TR process is shown in Figure 8 using a magenta dotted line for the PLB case. The final PLB signal obtained after the FCTF application $V_{REC}(t)$, is also plotted in Figure 8 with the black solid line. Similar to the reconstruction of the NBB signal, the FCTF application induced a shape and amplitude variation on the PLB signal. It is to be noted that Figure 8 shows only the shape variation since both signals before and after the FCTF application are normalized.

In the previously discussed NBB signals cases the authors knew what the outcome should be, as the authors engineered the signals being reconstructed to test the methodology. However, the PLB signal represents a real unknown BdB signal. That is why, for
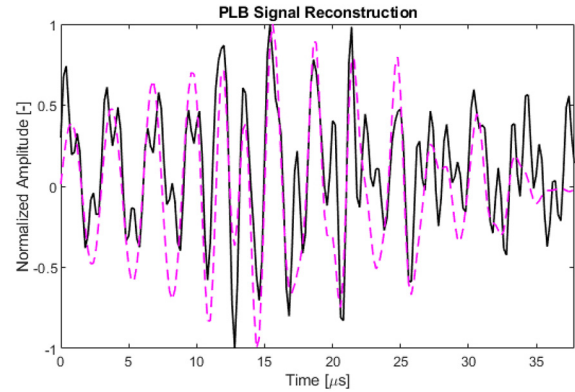
Figure 8. Isolated S_0 mode of the time-reversed output signal for the PLB case before (in magenta dotted) and after (in black) the aluminum FCTF application.


Figure 9. Comparisons between the S_0 mode of the reconstructed PLB signal (in magenta dotted) and the S_0 mode of the PLB signal experiment (red-dotted).

verification, the black signal in Figure 8 $V_{REC}(t)$ was amplified and sent from the PZT A to PZT R. The S_0 wave packet captured by PZT R, $V_{R-REC}(t)$ is shown in black in Figure 9 for the PLB case. In order to verify the effectiveness of the reconstruction at the first PZT, the black signal captured at the second PZT is compared with the real signal emitted by the PLB experiment $V_R(t)$ represented by the red dotted line in Figure 9. Furthermore, the correlation coefficient "r" is introduced for the two comparisons. The verification resulted in a high value of the correlation coefficient "r" (over 90%) as shown in Figure 9. This result suggests that the experimental FCTF method applied to a real BdB signal allows for the reconstruction of a single wave packet.

3.4. Numerical FCTF and BdB signal reconstruction

The FCTF was derived using the procedure developed in the first section of the methodology 2.1.1, and
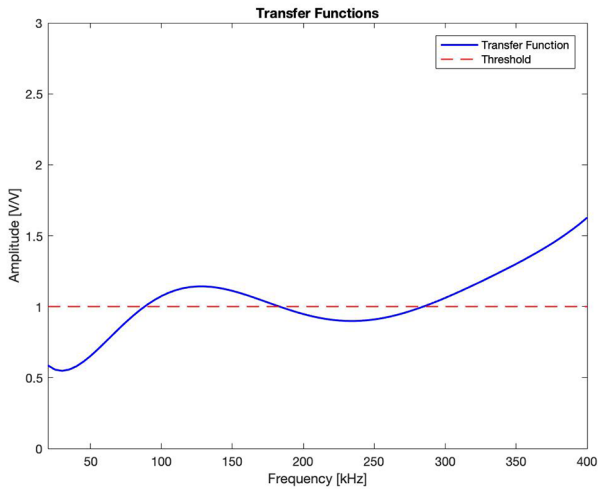
Figure 10. Transfer function obtained numerically with ABAQUS.

explained in Section 2.3.4 for the FEM application. The obtained vectors were interpolated in MATLAB™ using a seventh-order polynomial function. Figure 10 shows the interpolated functions in the range of interest up to 400 kHz. As seen in the same figure, the frequency ranges are modulated differently according to the relative transfer functions.
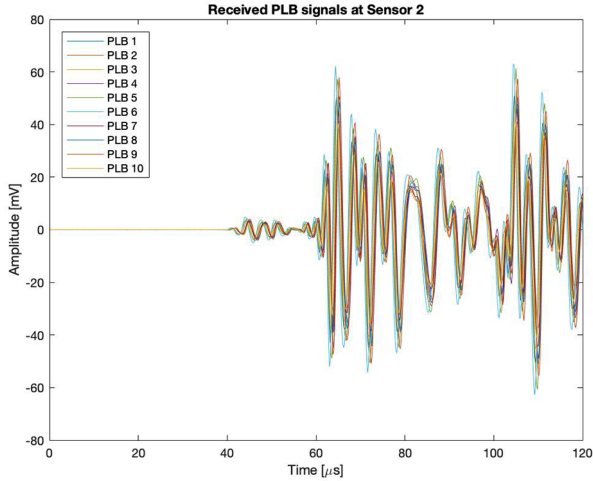
In comparing the aluminum FCTFs obtained numerically and experimentally, we can observe some similarities which can be highlighted in the typical AE frequency range below 400 kHz even though the numerical and experimental configurations are slightly different. Initially, at frequencies lower than 300 kHz, the FCTFs oscillate around the amplification/attenuation threshold as in the ABAQUS CAE™ model and in the experimental model of Figures 6(a) and 10 respectively. Above 300 kHz, both the numerical and experimental models present a high amplification. In particular, the experimental FCTF highlights the presence of an amplification peak at 350 kHz approximately.

The adopted procedure applies equation (5) and the result of this operation is shown in Figure 11 (from ABAQUS CAE™). The original NBB signal (blue solid line) in terms of voltage difference is compared with the reconstructed one before, Figure 11(a), and after, Figure 11(b), the application of the previously derived FCTF.

From Figure 11(a), it is possible to notice the effectiveness of time reversal of a broadband signal and the improvement when a broadband FCTF is applied to the reconstructed signal as seen in Figure 11(b). Moreover, this result is also confirmed by the correlation coefficient, denoted in the same figure as "*r*." Therefore, it is possible to make two important

(a)

(b)
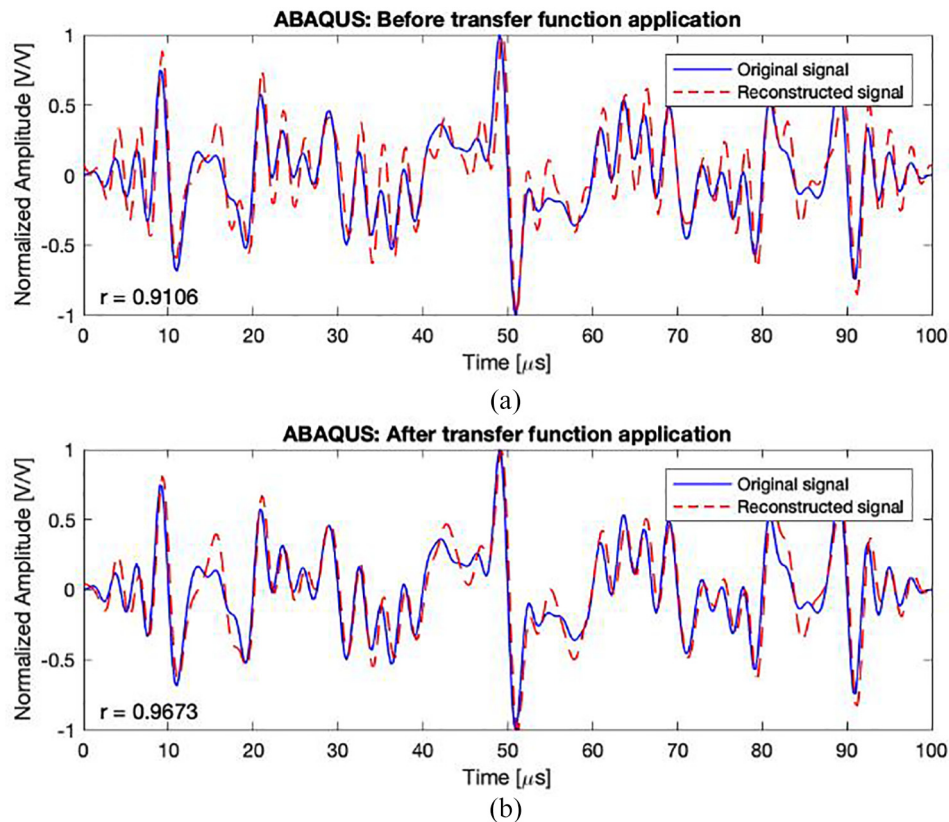
Figure 11. TR process applied to a broadband signal using the transfer function (ABAQUS™).

Figure 12. Plot of the 10 recorded PLB tests.

Figure 13. PLB reconstructed signals before (red dotted line) and after (blue solid line) FCTF application for ABAQUS™.

observations. First, even without the FCTF application, the reconstructed signal resembles the original one. Indeed, they have many features in common, such as time of arrival, amplitude or wave shape. Secondly, using the proposed methodology, it is possible to compensate for the distortion of the different frequency components.

3.5. Numerical PLB reconstruction

Figure 12 shows ten signals recorded at Sensor 2, Figure 4(a), to confirm the repeatability of the Hsu-Nielsen AE source.

The average between these signals was taken as input to complete the TR method numerically, emitting from Sensor 2 to 5 in the model, Figure 4(c). This procedure was repeated for the other 3 sensors. The results of the reconstructed PLB signal are shown in Figure 13, where the red dotted line represents the reconstruction before the FCTF application while the blue solid line represents the reconstructed PLB signal after the FCTF application at the source.

It is important to note that the application of the FCTF in this case does not change significantly the shape of the presumed "PLB signal," as depicted in Figure 13 by the red-dotted line and the blue solid line, especially if compared with the improved signal obtained applying the FCTF for the reconstruction of the NBB signal. This result could be associated with the fact that most of the energy of the PLB spectrum had a dominant frequency of 130 kHz for this setup. Therefore, in this case the FCTF becomes a constant function, scaling the received signal without altering its shape if the frequency of the signal is centralized around a single value.

A comparison between a numerical simulation using as input the previously reconstructed PLB signals and the received experimental PLB signals was performed,
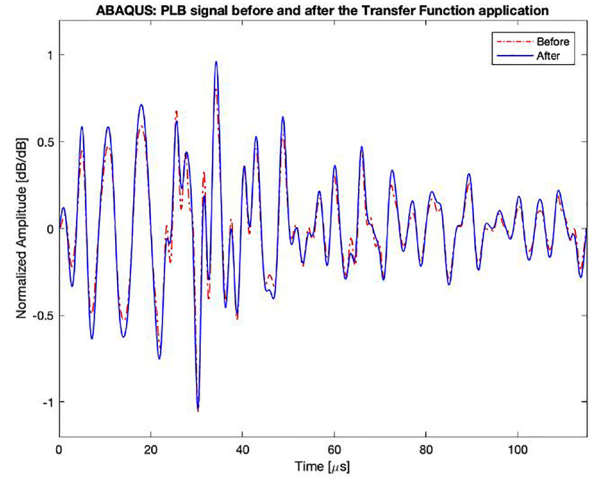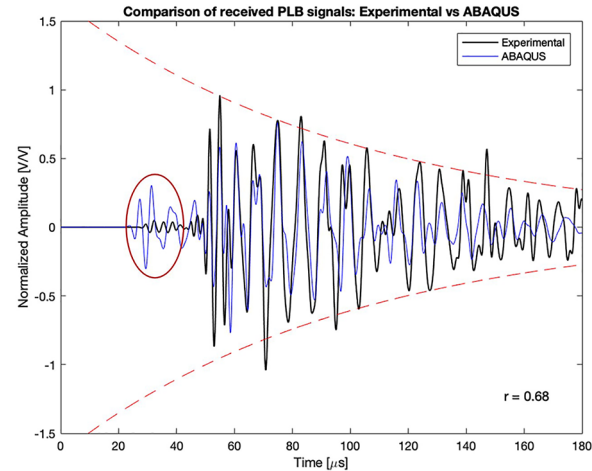
Figure 14. Experimental data compared with ABAQUS™ data received at PZT 4 using a PLB as AE source.

as shown in Figure 14. The experimental data consist of an average of the recorded PLB response at each of the four sensors. A cross correlation function was used for phase matching of the experimental and numerical signal and to assess quantitatively the similarity between the signals. Moreover, a lowpass filter was applied to the numerical PLB received signal in order to remove frequencies higher than 1.5 MHz. Figure 14 shows the received signal at Sensor 4, where the black and blue solid lines refer to the experimental and numerical received signals respectively.

In a first analysis, the damping behavior of numerical and experimental signals were compared. Wave attenuation was considered using the Rayleigh damping model available in ABAQUS CAE™. The mass and stiffness proportional damping coefficients were derived from experimental data performing PLB experiments.

In Figure 14, numerical and experimental results produced by a modeled and a real PLB AE respectively, show a similar exponential decay as indicated by the red-dotted line. Moreover, the two signals demonstrate to be in-phase with respect to each other. This comparison reflects the level of accuracy of the developed numerical model even though the cross-correlation coefficient of 0.68 was found with respect to the recorded experimental data. The lower cross-correlation value was due to the difference in S_0 wave packet (highlighted in Figure 14), which was much higher in the numerical model than in the experimental results. This could be due to several reasons such as the PZT tuning effect, which was not considered in the numerical model; and (or) the limitations of applying a Rayleigh damping model to Lamb waves. In theory, one should use different damping coefficients for every mode and for every frequency for an improved matching.

Modeling Lamb wave propagation, even a slight variation could cause a shift in phase or velocity, frequency dependent, causing error in the reconstructed signal at the end of the time reversal process.

The TR process requires identical conditions in the forward and backward propagations. A purely numerical TR process assures this requirement, even for a simplified model. On the contrary, time reversing signals generated by real AE and emitting them within the FEM model to complete the time reversal process, causes a discrepancy and the applied FCTF is not exactly representative of the interaction between the propagating waves and the structure. Therefore, the possible non-perfect correspondence between the numerically derived FCTF and the one associated with the real system in the experimental setup can be seen as an element to be further analyzed.

The results coming from the hybrid (numerical/experimental) methodology highlighted the potentiality and also the possible limitations of this study. The time-reversal process, enhanced with the application of the FCTF, can be applied to different material and for different sensor type and configurations. However, when the methodology was applied experimentally, the authors faced some practical limitations such as an upper limit in the signal length and sampling rate associated with the hardware characteristics and boundary reflections. Therefore, the authors' approach was done in steps, trying to apply the experimental methodology only to the S_0 wave packet. In the numerical methodology the authors made a step forward extending the procedure also to the asymmetric wave packet.

4. Conclusion

In this study the TR process related to BdB signals was analyzed and investigated. The objective was to extend the current state of art in the application of the TR process from simple NwB signals to BdB signals that in nature are comparable to real AE.

Analytical, experimental and numerical approaches in the application of the TR process were considered. The study was initially approached from an analytical point of view to understand the governing equations and derive a methodology for the FCTF. Several experiments were carried out under different sensor layouts, materials and type of signals in order to verify the consistency of the proposed methodology. As a further verification step, the same procedure was applied numerically with ABAQUS^{TM}, showing a good capability to reconstruct BdB signals. The obtained results open the possibility to develop a novel SHM algorithm for damage detection and identification building a library with the most likely occurring AE signals in operational conditions. Classical TR methodologies could now apply this scheme and implement the use of BdB instead of NwB signals in their algorithms. Even though the proposed methodology was effective in the numerical reconstruction, one of the limitations of this study was the difficulty in applying the time reversal methodology to the A_0 mode of the BdB signal experimentally. In future studies one possibility could be to derive two different transfer functions, one for the S_0 mode and another for the A_0 mode, exciting one mode per time exploiting the so-called sweet spot excitation or isolating the two modes by proper time-frequency analysis (i.e. wavelets decomposition).

ORCID iDs

Francesco Falcetelli 🔟 https://orcid.org/0000-0003-2820-776X
Marcias J Martinez 🔟 https://orcid.org/0000-0002-3985-9926

References

Adler L, de Billy M, Quentin G, et al. (1990) Evaluation of friction-welded aluminum-steel bonds using dispersive

guided modes of a layered substrate. *Journal of Applied Physics* 68(12): 6072–6076.

Anderson BE, Griffa M, Larmat C, et al. (2008) Time reversal. *Acoustics Today* 4(1): 5.

APC International (2019) *Physical and Piezoelectric Properties of APC Materials*. Available at: https://www.americanpiezo.com/apc-materials/piezoelectric-properties.html (accessed 10 November 2020).

ASTM International (2010) *ASTM E-976, Guide for Determining the Reproducibility of Acoustic Emission Sensor Response*. West Conshohocken, PA: ASTM International.

Balageas D, Fritzen C-P and Güemes A (ed.) (2006) *Structural Health Monitoring*. Newport Beach, CA: ISTE.

Barroso-Romero M, Gagar D, Pant S, et al. (2019) Wave mode identification of acoustic emission signals using phase analysis. *Acoustics* 1(2): 450–472.

Benmedakhene S, Kenane M and Benzeggagh ML (1999) Initiation and growth of delamination in glass/epoxy composites subjected to static and dynamic loading by acoustic emission monitoring. *Composites Science and Technology* 59(2): 201–208.

Bhuiyan MY, Bao J, Poddar B, et al. (2018) Toward identifying crack-length-related resonances in acoustic emission waveforms for structural health monitoring applications. *Structural Health Monitoring* 17(3): 577–585.

Boczar T and Lorenc M (2006) Time-frequency analysis of the calibrating signals generated in the hsu-nielsen system. *Physics and Chemistry of Solid State* 7: 585–588.

Cassereau D and Fink M (1992) Time-reversal of ultrasonic fields. III. Theory of the closed time-reversal cavity. *IEEE Transactions on Ultrasonics, Ferroelectrics and Frequency Control* 39(5): 579–592.

Cawley P and Alleyne D (1996) The use of lamb waves for the long range inspection of large structures. *Ultrasonics* 34(2–5): 287–290.

Diamanti K, Hodgkinson JM and Soutis C (2004) Detection of low-velocity impact damage in composite plates using lamb waves. *Structural Health Monitoring: An International Journal* 3(1): 33–41.

Dunegan HL (2000) *An Alternative to Pencil Lead Breaks for Simulation of Acoustic Emission Signal Sources*. The DECI report.

Dunegan HL, Harris DO and Tatro CA (1968) Fracture analysis by use of acoustic emission. *Engineering Fracture Mechanics* 1(1): 105–122.

Falcetelli F, Romero MB, Pant S, et al. (2018) Modelling of pencil-lead break acoustic emission sources using the time reversal technique. In: *EWSHM 2018*, Manchester, UK, 10–13 July 2018. NDT.net. Available at: https://www.ndt.net/article/ewshm2018/papers/0367-Falcetelli.pdf

Farrar CR and Worden K (2007) An introduction to structural health monitoring. *Philosophical Transactions of the Royal Society A: Mathematical, Physical and Engineering Sciences* 365(1851): 303–315.

Fink M (1992) Time reversal of ultrasonic fields. Basic principles. *IEEE Transactions on Ultrasonics, Ferroelectrics and Frequency Control* 39(5): 555–566.

Fink M (1997) Time reversed acoustics. *Physics Today* 50(3): 34–40.

Giurgiutiu V (2005) Tuned lamb wave excitation and detection with piezoelectric wafer active sensors for structural health monitoring. *Journal of Intelligent Material Systems and Structures* 16(4): 291–305.

Gresil M and Giurgiutiu V (2015) Prediction of attenuated guided waves propagation in carbon fiber composites using Rayleigh damping model. *Journal of Intelligent Material Systems and Structures* 26(16): 2151–2169.

Hsu NN and Breckenridge FR (1981) Characterization and calibration of acoustic emission sensors. *Materials Evaluation* 39: 60–68.

Ing RK and Fink M (1998) Time-reversed lamb waves. *IEEE Transactions on Ultrasonics, Ferroelectrics and Frequency Control* 45(4): 1032–1043.

Lamb H (1917) On waves in an elastic plate. *Proceedings of the Royal Society of London. Series A, Containing Papers of a Mathematical and Physical Character* 93(648): 114–128.

Martin SA and Blackshire JL (2007) Effect of adhesive properties on elastic wave generation by bonded sensors. In: *The 14th International symposium on: Smart structures and materials & nondestructive evaluation and health monitoring* (ed. KJ Peters), San Diego, CA, 6 April 2007, p.65300J.

Martinez M, Pant S, Yanishevsky M, et al. (2017) Residual stress effects of a fatigue crack on guided lamb waves. *Smart Materials and Structures* 26(11): 115004.

Moser F, Jacobs LJ and Qu J (1999) Modeling elastic wave propagation in waveguides with the finite element method. *NDT & E International* 32(4): 225–234.

Moulin E, Assaad J, Delebarre C, et al. (2000) Modeling of integrated lamb waves generation systems using a coupled finite element–normal modes expansion method. *Ultrasonics* 38(1–8): 522–526.

Mulligan KR, Masson P, Létourneau S, et al. (2011) An approach to compensate for the degradation of the monitoring system in damage detection. In: *Smart Materials & Structures | NDT in Aerospace*, Montreal, QC, Canada, 2–4 November 2011.

Pant S, Laliberte J, Martinez M, et al. (2014) Derivation and experimental validation of Lamb wave equations for an n-layered anisotropic composite laminate. *Composite Structures* 111: 566–579.

Park HW, Kim SB and Sohn H (2009) Understanding a time reversal process in lamb wave propagation. *Wave Motion* 46(7): 451–467.

Pettit JR, Walker A, Cawley P, et al. (2014) A stiffness reduction method for efficient absorption of waves at boundaries for use in commercial finite element codes. *Ultrasonics* 54(7): 1868–1879.

PicoTechnology (2016) *PicoScope 6 PC Oscilloscope Software User's Guide*. Available at: https://www.picotech.com/download/manuals/picoscope6-oscilloscope-software-users-guide.pdf (accessed 10 November 2020).

Piezo-Kinetics (2016) *Material Specifications*. Available at: https://piezo-kinetics.com/wp-content/uploads/2017/04/pki-specs-2016-1.pdf (accessed 10 November 2020).

Poddar B, Kumar A, Mitra M, et al. (2011) Time reversibility of a lamb wave for damage detection in a metallic plate. *Smart Materials and Structures* 20(2): 025001.

Qing XP, Chan H-L, Beard SJ, et al. (2006) Effect of adhesive on the performance of piezoelectric elements used to monitor structural health. *International Journal of Adhesion and Adhesives* 26(8): 622–628.

Roberts TM and Talebzadeh M (2003) Acoustic emission monitoring of fatigue crack propagation. *Journal of Constructional Steel Research* 59(6): 695–712.

Rose LRF and Wang CH (2004) Mindlin plate theory for damage detection: Source solutions. *The Journal of the Acoustical Society of America* 116(1): 154–171.

Sause MGR (2011) Investigation of pencil lead breaks as acoustic emission sources. *Journal of Acoustic Emission* 29: 184–196.

Sohn H, Park HW, Law KH, et al. (2007a) Combination of a time reversal process and a consecutive outlier analysis for baseline-free damage diagnosis. *Journal of Intelligent Material Systems and Structures* 18(4): 335–346.

Sohn H, Park HW, Law KH, et al. (2007b) Damage detection in composite plates by using an enhanced time reversal method. *Journal of Aerospace Engineering* 20(3): 141–151.

Su Z and Ye L (2009) Identification of damage using lamb waves. In: *Lecture Notes in Applied and Computational Mechanics*. London: Springer.

Vallen Systeme (2019) *VS900-M*. Available at: https://www.vallen.de/sensors/broad-band-sensors/vs900-m/ (accessed 10 November 2020).

Von Hann J (1903) *Handbook of Climatology*. New York; London: Macmillan.

Wagle S and Kato H (2009) Ultrasonic detection of fretting fatigue damage at bolt joints of aluminum alloy plates. *International Journal of Fatigue* 31(8–9): 1378–1385.

Wang CH, Rose JT and Chang F-K (2003) Computerized time-reversal method for structural health monitoring. In: *NDE for Health Monitoring and Diagnostics* (eds Gyekenyesi AL and Shull PJ), San Diego, CA, 4 August 2003, p. 48.

Wang J and Shen Y (2019) An enhanced lamb wave virtual time reversal technique for damage detection with transducer transfer function compensation. *Smart Materials and Structures* 28(8): 085017.

Xu B and Giurgiutiu V (2007) Single mode tuning effects on lamb wave time reversal with piezoelectric wafer active sensors for structural health monitoring. *Journal of Nondestructive Evaluation* 26(2–4): 123–134.